Numerical simulation of viscous air dynamics in emphysemic human lungs

Cite as: AIP Advances 15, 105022 (2025); doi: 10.1063/5.0293120
Submitted: 25 July 2025 • Accepted: 29 September 2025 •
Published Online: 15 October 2025

Nilufar Yasmin,[1,2,a)] Roni Akter,[2] Mst. Sathi Akter,[3] and Mahtab U. Ahmmed[2]

AFFILIATIONS

[1] Department of MPS (Mathematical & Physical Sciences), East West University, Dhaka 1212, Bangladesh
[2] Department of Mathematics, Jahangirnagar University, Dhaka 1342, Bangladesh
[3] Department of Mathematics, Uttara University, Dhaka 1230, Bangladesh

Note: This paper is part of the Special Topic on Advances in Fluid Dynamics and Applied Fluid Physics.
[a)] **Author to whom correspondence should be addressed:** nilufaryasmin272@gmail.com

ABSTRACT

Emphysema is a chronic lung condition characterized by the destruction of alveolar walls, leading to abnormal air trapping and reduced airflow. This study presents a numerical simulation of airflow dynamics in emphysemic lungs using a porous media approach to model deformed lung structure. The governing equations for air and particle transport were solved using a finite difference scheme under pulsatile flow conditions. We solve these equations using the finite difference method in MATLAB. Key flow parameters such as Reynolds number, porosity, and particle drag were varied to analyze their impact on airflow and dust movement. Simulation results show that both air and dust particle velocities increase with Reynolds number due to reduced viscous resistance and stronger inertial effects, even within a low-Re regime. The porous medium model effectively captures the impaired ventilation and altered flow distribution observed in emphysematous lungs. This work contributes to better understanding of airflow mechanics in diseased lung tissue and can aid future research in drug delivery or particle deposition in respiratory disorders.

I. INTRODUCTION

Lung diseases remain one of the leading causes of death worldwide, impacting millions of people each year and contributing to a substantial number of annual fatalities.[1] Blood oxygenators, also known as artificial lungs, are commonly utilized to support patients experiencing lung disease or respiratory failure.[2] Recent advancements in blood gas exchangers have focused on multifunctional respiratory support, improving their efficiency in replacing or supplementing lung function.[3] The respiratory system, which includes the lungs, is where air-breathing vertebrates like humans do their respiration. Inhalation is the action of forcing air into the lungs to bring oxygen to the body, while exhalation is the action of forcing air out of the lungs to remove carbon dioxide. This process referees breathing or ventilation. A computational framework for particle installation by the joint mechanisms of sedimentation and diffusion reported by Sturm and Hofmann [Sturm] used various emphysema models for 0.001–10 m particles from generations 12 to alveoli. When compared to models reflecting different forms of emphysema, they discovered that the healthy model had more particle deposition. Some researchers conducted experimental research on a scale-up model of an alveolus that expands and contracts rhythmically and is installed on a straight duct with a constant, unidirectional flow. They discovered that rhythmic wall motion significantly altered the flow properties. Considering a magnetic field and viscous dissipation, Sankar conducted the same work as Girish *et al.* in the perpendicular double-passage porous annuli. In addition, Sankar *et al.* discussed vertical annular laminar regular double-diffusive convection with free end and an unheated entry and exit.[4] Amit *et al.* most recent study found that while septal damage reduces flow resistance through the alveolar ducts, it does not affect the bulk transit of oxygen into the alveoli.

The respiratory bronchioles are an essential component of the respiratory system, playing a vital role in ensuring oxygen is delivered to the body's tissues and carbon dioxide is efficiently eliminated from the body. According to respirational function and its anatomical configuration, the lungs consist of two regions called air transport and gas diffusion. The airways from the trachea to terminal bronchioles are fractionalized repeatedly and gas is delivered without any gas exchange.[5]

Most of the research in the literature concentrates on the flow activity in an emphysema-affected lung by taking into the rupture of the septal wall. In contrast, some researches focused on the installation of spherical particles in an emphysema-affected lung. The porous nature of emphysematous lungs and the impact of particle shape on the deposit have received no attention. These fundamental truths are still incredibly little understood. It is, therefore, our goal to close this limitation.

In our discussion, pulsatile fluid flow is investigated in two-dimensional, emphysemic, and healthy alveolar sac model geometries with rhythmic breathing conditions. The flow state of an emphysema-affected lung is described by the generalized Navier–Stokes equation for a porous medium. In addition, particle trajectories with particle form factors are calculated using the Newton second equation of motion. In addition, the effects of $0.2\leq$ Reynolds number ≤ 1; $10\leq$ aspect ratio≤ 25; and $0.1\leq$ Darcy number ≤ 0.001, $0.84\leq$ media porosity ≤ 2 are considered.

II. MATHEMATICAL MODEL

Inspiration and expiration are vital processes that allow the body to release carbon dioxide and deliver oxygen to tissues.[6] The lungs are a crucial component of this system. Researchers and medical professionals interested in all types of respiratory illnesses are very interested in the study of airflow in the lungs. There are few in vitro and in vivo methods for researching this flow regime.[7] The size of the particle determines how it is distributed throughout the lung airways. Particles smaller than those of larger sizes are spread uniformly.[8] Here, an alveolar duct linked to a single alveolus is illustrated in Fig. 1, which helps visualize the distribution of airflow and particles in the lung.

A. Governing equations

An incompressible, fully developed, steady, laminar flow of a Newtonian fluid occurs along the axis of a tube, subjected to an oscillatory boundary condition and a time-dependent pressure gradient. A mathematical model proposed by Saini *et al.*[9] is considered here

Equation of continuity,

$$\frac{\partial u_x}{\partial x} + \frac{u_x}{x} + \frac{\partial u_y}{\partial y} = 0, \tag{1}$$

$$\frac{\partial v_x}{\partial x} + \frac{v_x}{x} + \frac{\partial v_y}{\partial y} = 0. \tag{2}$$

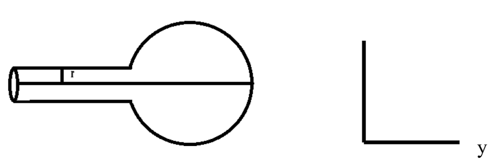

FIG. 1. Diagram of an alveolar duct linked to a single alveolus.

Equation of radial momentum,

$$\frac{\partial u_x}{\partial t} + \frac{u_x}{\varepsilon}\frac{\partial u_x}{\partial x} + \frac{u_y}{\varepsilon}\frac{\partial u_x}{\partial y} = -\frac{\varepsilon}{\rho_a}\frac{\partial p}{\partial x} + \nu\left(\frac{\partial^2 u_x}{\partial x^2} + \frac{1}{x}\frac{\partial u_x}{\partial x} + \frac{\partial^2 u_x}{\partial y^2}\right) + \left(-\frac{\varepsilon\nu}{K}u_x + k_f\frac{\rho_p}{\rho_a}(v_x - u_x)\right). \tag{3}$$

Equation of axial momentum,

$$\frac{\partial u_y}{\partial t} + \frac{u_x}{\varepsilon}\frac{\partial u_y}{\partial x} + \frac{u_y}{\varepsilon}\frac{\partial u_y}{\partial y} = -\frac{\varepsilon}{\rho_a}\frac{\partial p}{\partial y} + \nu\left(\frac{\partial^2 u_y}{\partial x^2} + \frac{1}{x}\frac{\partial u_y}{\partial x} + \frac{\partial^2 u_y}{\partial y^2}\right) + \left(-\frac{\varepsilon\nu}{K}u_y + k_f\frac{\rho_p}{\rho_a}(v_y - u_y)\right). \tag{4}$$

K[10] is called permeability and depends on the porosity ε[11] as follows:

$$K = \frac{\varepsilon^3 {d_p}^2}{150(1-\varepsilon)^2}. \tag{5}$$

In a person with emphysema, the total lung capacity (TLC) is the maximum amount of air the lungs can hold after a deep breath. However, the tidal volume—the air breathed in and out during normal breathing—becomes smaller. This is because the lungs are already overfilled with trapped air and cannot expand properly to take in fresh air. When the person tries to breathe out, they cannot fully empty their lungs because a lot of air stays inside—this is called residual volume.

Because of this, we can measure how well the lungs can exchange air—known as lung porosity—by using the tidal volume, as explained in the following:

$$\text{porosity}(\varepsilon) = \frac{\text{tidal lung volume } (v_t)}{\text{total volume } (V)},$$
$$\text{and } k_f = 3\pi\mu C_f d_f,\ [10], \tag{6}$$
$$C_f = 1 - \frac{\lambda}{d_p}\left[2.514 + 0.800 \exp\left(\frac{-0.55\cdot d_p}{\lambda}\right), \lambda = 0.066\ \mu\text{m}\right],$$

where C_f[12] stands for the Cunningham slip correction factor, which is used for very small (thin) particles, and d_p is the diameter of the elongated nanoparticle. Using these, the formula for the aerodynamic diameter[10] becomes simpler and can be written as follows:

$$d_p = d\left(\frac{\rho_p}{S_f\rho_0}\right)^{1/2}.$$

A factor called the particle shape factor (S_f) is used to understand how non-spherical particles move and settle in the air. It is calculated using the formula,

$$S_f = \frac{1}{3}\left(\frac{2}{S_\parallel} + \frac{1}{S\perp}\right).$$

A simple, practical idea about how (S_f) depends on particle orientation was introduced by Su and Cheng.[13] They explained that $S_\perp$ is used when a particle's long axis is perpendicular (upright) to the airflow, and $S_\parallel$ is used when the long axis is parallel to the airflow.

Mathematically, $S_\perp$ and $S_\parallel$ are given by

$$S_\perp = \frac{\frac{8}{3}(\beta^2-1)\beta^{\frac{-1}{3}}}{\left(\frac{(2\beta^2-3)}{(\beta^2-1)^{\frac{1}{2}}}\right)\ln\left(\beta+(\beta^2-1)^{\frac{1}{2}}\right)+\beta}.$$

$$S_\parallel = \frac{\frac{4}{3}(\beta^2-1)\beta^{\frac{-1}{3}}}{\left(\frac{(2\beta^2-3)}{(\beta^2-1)^{\frac{1}{2}}}\right)\ln\left(\beta+(\beta^2-1)^{\frac{1}{2}}\right)-\beta},$$

where β denotes the aspect ratio.

Equation of particle motion in axial direction,

$$\frac{\partial v_y}{\partial t} + v_y\frac{\partial v_y}{\partial y} + v_x\frac{\partial v_y}{\partial x} = \frac{F_{d_2}}{m}. \tag{7}$$

B. Initial and boundary conditions

This study uses the following initial and boundary conditions at $t = 0$.

(1) There is no flow when we consider that the flow is at rest,

$$u_x = v_x = u_y = v_y = 0. \tag{8}$$

(2) We consider no radial flow over the axial direction of the alveolar tube. So, the axial velocity gradient is measured to zero,

$$u_x = 0,\ v_x = 0,\ \frac{\partial u_x}{\partial x} = 0,\ \frac{\partial v_y}{\partial x} = 0. \tag{9}$$

(3) On the inside of the wall, no-slip condition is imposed.

III. MATHEMATICAL SOLUTIONS

A. Transformation of the governing equations

To illustrate the above-mentioned equations numerically, we construct the dimensionless form by introducing some non-dimensional quantities,

$$\begin{gathered} X^* = \frac{x}{r},\quad Y^* = \frac{y}{r},\quad p^* = \frac{P}{\rho_a {U_0}^2},\quad \tau^* = \frac{t}{t_0},\\ {U_x}^* = \frac{u_x}{U_0},\quad {U_y}^* = \frac{u_y}{U_0},\quad {V_x}^* = \frac{v_x}{U_0},\\ {V_y}^* = \frac{v_y}{U_0},\quad D_a = \frac{K}{r^2},\quad P_l = \frac{\rho_p}{\rho_a},\\ S_m = \frac{rk_f}{U_0},\quad \mathrm{Re} = \frac{rU_0}{\nu},\quad S_t = \frac{r}{U_0 t_0}, \end{gathered} \tag{10}$$

where r is radius of the circular tube, R_e is the Reynolds number, U_0 is initial velocity, t_0 is initial time, and S_t is Strouhal number. Using the mentioned quantities, our assumptions, and information from the continuity Eqs. (1) and (2), we get

$$\frac{\partial U_x}{\partial X} + \frac{U_x}{X} + \frac{\partial U_y}{\partial Y} = 0 \tag{11}$$

and

$$\frac{\partial V_x}{\partial X} + \frac{V_x}{X} + \frac{\partial V_y}{\partial Y} = 0. \tag{12}$$

The equation of axial momentum (4) becomes

$$\begin{aligned} \Rightarrow S_t\frac{\partial U_y}{\partial \tau} + \frac{U_x}{\varepsilon}\frac{\partial U_y}{\partial X} + \frac{U_y}{\varepsilon}\frac{\partial U_y}{\partial Y} &= -\frac{\varepsilon}{\rho_a}\frac{\partial p}{\partial y} + \frac{1}{Re}\left(\frac{\partial^2 U_y}{\partial X^2} + \frac{1}{X}\frac{\partial U_y}{\partial X} + \frac{\partial^2 U_y}{\partial Y^2}\right)\\ &\quad + p_l S_m(V_y - U_y) - \frac{\varepsilon}{D_a \mathrm{Re}}U_y. \end{aligned} \tag{13}$$

Since

$$\frac{U_0 r}{\upsilon} = \frac{1}{Re} \quad \text{and} \quad D_a = \frac{K}{r^2} \quad \text{and} \quad \frac{\rho_p}{\rho_a} = p_l.$$

In addition, equation of particle motion in axial direction (7) becomes

$$\begin{aligned} \Rightarrow S_t\frac{\partial V_y}{\partial \tau} + V_y\frac{\partial (V_y)}{\partial (Y)} + (V_x)\frac{\partial (V_y)}{\partial (X)} &= \frac{S_m S_f(U_y - V_y)}{m} \quad \left[\frac{rk_f}{U_0} = S_m\right]. \end{aligned} \tag{14}$$

Equations (11)–(14) are the lung model equations. Now, we want to solve Eqs. (13) and (14) for finding the axial velocity of air and dust particles.

IV. DISCRETIZATION OF THE MODEL EQUATIONS

A. Axial velocity of air particles

We employed the FTCSCS technique to determine the axial velocity of airborne particles.

Choosing a mesh width $\Delta x, \Delta y$ for the space variable and $\Delta\tau$ for the time variable will discretize the plane. The approximate solution at grid points for axial velocity of fluid $U(X,Y,t)$ and particles $V(X,Y,t)$ are expressed as $U_y(X_i,Y_j,\tau_n)$ or $(U_y)^n_{i,j}$ and $V_y(X_i,Y_j,\tau_n)$ or $(V_y)^n_{i,j}$, respectively,

$$\begin{aligned} &U_y(X_i,Y_j,\tau_n) \ \text{or}\ (U_y)^n_{i,j}\cdot\ \ \text{Where,}\\ &X_i = i\Delta x,\quad i = 0,1,2,3\ldots\ldots\ldots\ldots N,\\ &Y_j = j\Delta y,\quad j = 0,1,2,3\ldots\ldots\ldots\ldots N,\\ &\tau_n = (n-1)\Delta\tau,\quad n = 1,2,3\ldots\ldots\ldots\ldots \end{aligned}$$

Here, $i, j, and\ n$ are radial and axial time indices, respectively. $\Delta X, \Delta Y\ and\ \Delta\tau$ are the length for spatial variables and length for temporal variable, respectively. We approximated with central difference methods, for all the special derivatives, as follows:

$$\begin{aligned} \frac{\partial U_y}{\partial Y} &= \frac{(U_y)^n_{i,j+1} - (U_y)^n_{i,j-1}}{2\Delta Y} + o(\Delta Y)^2,\\ \frac{\partial U_y}{\partial Y} &\approx \frac{(U_y)^n_{i,j+1} - (U_y)^n_{i,j-1}}{2\Delta Y}, \end{aligned} \tag{15}$$

$$\frac{\partial U_y}{\partial X} = \frac{(U_y)^n_{i,j+1} - (U_y)^n_{i,j-1}}{2\Delta X} + o(\Delta X)^2, \quad \frac{\partial U_y}{\partial X} \approx \frac{(U_y)^n_{i,j+1} - (U_y)^n_{i,j-1}}{2\Delta X}. \tag{16}$$

For time and space derivatives, the second-order central difference approximation is as follows:

$$\frac{\partial^2 U_y}{\partial Y^2} = \frac{(U_y)^n_{i,j+1} - 2(U_y)^n_{i,j} + (U_y)^n_{i,j-1}}{\Delta Y^2} + o(\Delta Y)^2, \quad \frac{\partial^2 U_y}{\partial Y^2} \approx \frac{(U_y)^n_{i,j+1} - 2(U_y)^n_{i,j} + (U_y)^n_{i,j-1}}{\Delta Y^2}, \tag{17}$$

$$\frac{\partial^2 U_y}{\partial X^2} = \frac{(U_y)^n_{i,j+1} - 2(U_y)^n_{i,j} + (U_y)^n_{i,j-1}}{\Delta X^2} + o(\Delta X)^2, \quad \frac{\partial^2 U_y}{\partial X^2} \approx \frac{(U_y)^n_{i,j+1} - 2(U_y)^n_{i,j} + (U_y)^n_{i,j-1}}{\Delta X^2}. \tag{18}$$

In addition, at point (X_i, Y_i, τ_n), for time derivative, we applied first-order forward difference approximation as follows:

$$\frac{\partial U_y}{\partial \tau} = \frac{(U_y)^{n+1}_{i,j} - (U_y)^n_{i,j}}{\Delta \tau} + o(\Delta\tau), \quad \frac{\partial U_y}{\partial \tau} \approx \frac{(U_y)^{n+1}_{i,j} - (U_y)^n_{i,j}}{\Delta \tau}. \tag{19}$$

Substituting these in Eq. (13), we get axial velocity at $0 < x \le 1$ and has its discretized form as

$$\begin{aligned}(U_y)^{n+1}_{i,j} ={}& (U_y)^n_{i,j}\left[1 - 2\frac{\Delta\tau}{ReS_t\Delta X^2} - 2\frac{\Delta\tau}{ReS_t\Delta Y^2} - \frac{\varepsilon\Delta\tau}{D_a\mathrm{Re}S_t} - S_mP_l\frac{\Delta\tau}{S_t}\right] - \frac{\Delta\tau}{S_t\,\varepsilon 2\Delta X}\left[(U_x)^n_{i,j}(U_y)^n_{i+1,j} - (U_x)^n_{i,j}(U_y)^n_{i-1,j}\right]\\ &- \frac{\Delta\tau}{S_t\,\varepsilon 2\Delta Y}\left[(U_y)^n_{i,j}(U_y)^n_{i,j+1} - (U_y)^n_{i,j}(U_y)^n_{i,j-1}\right] + \frac{\Delta\tau}{ReS_t\Delta Y^2}\left[(U_y)^n_{i,j+1} - (U_y)^n_{i,j-1}\right] - \frac{\varepsilon\Delta\tau}{S_t}\cdot\left[\exp\left(-\frac{\alpha' tr}{U_0}\right) + s_f\right]\\ &+ (U_y)^n_{i+1,j}\left[\frac{\Delta\tau}{ReS_t\Delta X^2} + \frac{\Delta\tau}{ReS_tx2\Delta X}\right] + (U_y)^n_{i-1,j}\left[\frac{\Delta\tau}{ReS_t\Delta X^2} - \frac{\Delta\tau}{ReS_tx2\Delta X}\right] + S_mP_l\frac{\Delta\tau}{S_t}(V_y)^n_{i,j},\end{aligned} \tag{20}$$

which is the required FTCSCS scheme for axial velocity of air particles

B. Axial velocity of dust particles

Now, we applied first-order forward difference approximation for time derivative,

$$\frac{\partial V_y}{\partial \tau} \approx \frac{(V_y)^{n+1}_{i,j} - (V_y)^n_{i,j}}{\Delta \tau} + o(\Delta\tau), \quad \frac{\partial V_y}{\partial \tau} \approx \frac{(V_y)^{n+1}_{i,j} - (V_y)^n_{i,j}}{\Delta \tau}. \tag{21}$$

Then, we applied second-order central difference approximation for space derivative,

$$\frac{\partial V_y}{\partial Y} = \frac{(V_y)^n_{i,j+1} - (V_y)^n_{i,j-1}}{2\Delta Y} + o(\Delta Y)^2, \quad \frac{\partial V_y}{\partial Y} \approx \frac{(V_y)^n_{i,j+1} - (V_y)^n_{i,j-1}}{2\Delta Y}, \tag{22}$$

and also, second-order central difference approximation for space derivative,

$$\frac{\partial V_y}{\partial X} = \frac{(V_y)^n_{i+1,j} - (V_y)^n_{i-1,j}}{2\Delta X} + o(\Delta X)^2, \quad \frac{\partial V_y}{\partial X} \approx \frac{(V_y)^n_{i+1,j} - (V_y)^n_{i-1,j}}{2\Delta X}. \tag{23}$$

Using (21)–(23), we get from (14),

$$\begin{aligned}(V_y)^{n+1}_{i,j} ={}& (V_y)^n_{i,j}\left[1 - \frac{S_mS_f\Delta\tau}{mS_t}\right] + \frac{S_mS_f\Delta\tau}{mS_t}(U_y)^n_{i,j}\\ &- \frac{\Delta\tau}{S_t.2\,\Delta x}(V_x)^n_{i,j}\left[(V_y)^n_{i+1,j} - (V_y)^n_{i-1,j}\right]\\ &- \frac{\Delta\tau}{S_t.2\,\Delta x}(V_y)^n_{i,j}\left[(V_y)^n_{i,j+1} - (V_y)^n_{i,j-1}\right],\end{aligned} \tag{24}$$

which is the required FTCSCS scheme for axial velocity of dust particles.

V. MODEL VALIDATION AND GRID INDEPENDENCY

A grid independence test was carried out before analyzing the current problem to determine the model's prediction accuracy by examining several grid sizes 21 × 21, 31 × 31 100 × 100, in an axial direction. A grid independence test along with a numerical code validation was carried out. We got the results to remain consistent when the grid size is 31 × 31, when we choose the time step to be $\Delta\tau = 0.001$, $\Delta X = 0.01$ and $\Delta Y = 0.01$ along the axial direction.

A. Computational stability

In order to obtain the air (U_y) and particle (V_X) velocities, the above-mentioned equations are solved explicitly by using the defined discretization methods, and the stability condition for the schemes is shown in the following:

$$\max\left\{\frac{\Delta\tau}{\Delta X^2}\right\} \le 0.5.$$

The results seem to be converging with order 10^{-3} precision.[10]

VI. RESULT AND DISCUSSION

The governing equations defined by (1)–(4), (7), and (8) are controlled by the parameters—Reynolds numbers(Re), Darcy number (D_a), aspect ratio(β), Womersley number(α), Strouhal numbe r (S_t), breathing rate(α'), and porosity(ε) and we also wanted to compare a normal lung to an emphysema-damaged lung to see how the disease affected the lungs. Since the respiratory bronchioles or transitional bronchioles of the 18th generation of the lung exchange more gas, we evaluated this generation.

Under this generation, to evaluate the effect of the above-mentioned parameters, numerical quantities are defined by the chart shown in Table I,[14–16]

where 0.2≤ Reynolds number ≤1; 15≤ aspect ratio≤ 2; and 0.1≤ Darcy number ≤0.001, 0.84≤ media porosity ≤2 are considered.

A. Mesh generation for the axial velocity of air particles

Assume the respiratory length of the bronchial tube as the y axis and its diameter or radial distance as the x axis. We split the domain 51 times along the y axis and 51 times along the x axis since the respiratory bronchial tube's length is around 1.2 mm, and its diameter is ~0.5 mm under the 18th generation of the bronchial tube. Then, using 1000 nodes for time and Re = 0.2, D_a = 0.01, $\varepsilon = 0.84, \alpha' = 12, \beta = 10$, we calculate the mesh for the axial velocity of fluid and dust particles at 1 s.

As a result, the fluid mesh employing the FTCSCS scheme is obtained (Fig. 2), and the corresponding dust particle mesh is shown in Fig. 3.

A portion of inspired air travels in the axial direction to distal airways due to alveolar expansion during inhalation, whereas the remaining amount travels in the radial direction. We noticed that the axial and radial air particle velocities exhibit a parabolic curve. Flow field and aerosol deposition problems were accurately solved with this mesh size.

We observed that dust particle velocities in the axial and radial directions also exhibit a parabolic curve.

B. Contour of the flow field

According to Figs. 4 and 5, the axial velocity profile of fluid(air) and dust particles is high in the area of dark red color, and it is low in the area of dark blue color because the air and particles have already diffused there. As per contour figures, the axial velocity of air and dust particles decreases with both the radial and axial distance. On the axis and radius of tubes, respectively, the air moves at its fastest speed and the dust particles move at its slowest speed.

Here, the right-hand color bar represents the measurement of velocity of flow field of tube.

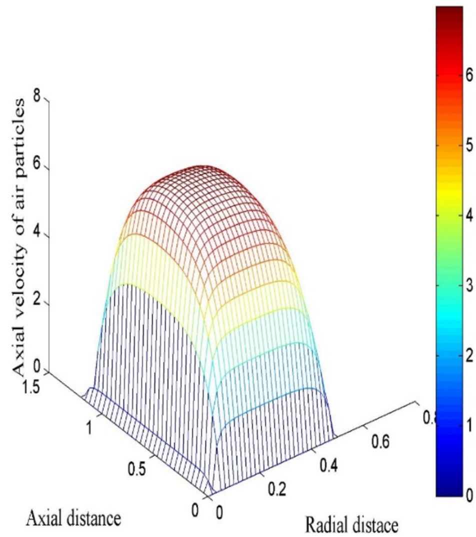

FIG. 2. Mesh for axial velocity for air particles.

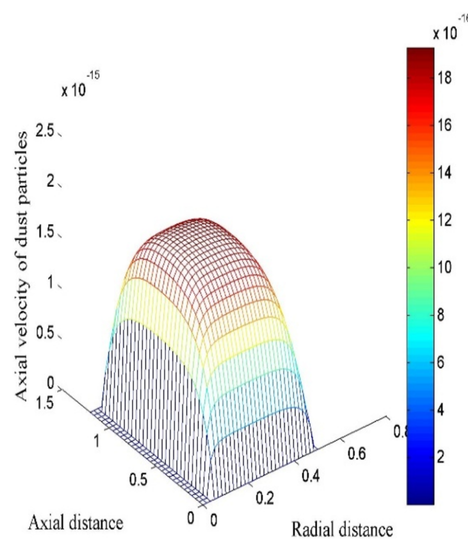

FIG. 3. Mesh for axial velocity for dust particles.

TABLE I. Value of parameters.

Variable	Value
Mass(m)	0.0002 kg/I
Diameter of sphere of unite density(d)	100 nm
Frequency (f)	1.2 Hz
Density of the particles (ρ_p)	$0.025\,04 \times 10^{12}$ m^3
Density of the air (ρ_a)	1.145 kg/m^3
Kinematic viscosity (υ)	1.71×10^{-5} m^3/s
Radius(r)	125 μm
Velocity (U)	0.3 m/s

C. Velocity profiles of air and dust particles

Figures 6 and 7 shows velocity variation (axial) of air and dust particles along the axial direction at different radial positions. In Fig. 6, the curve shown by the line (red) denotes the axial velocity

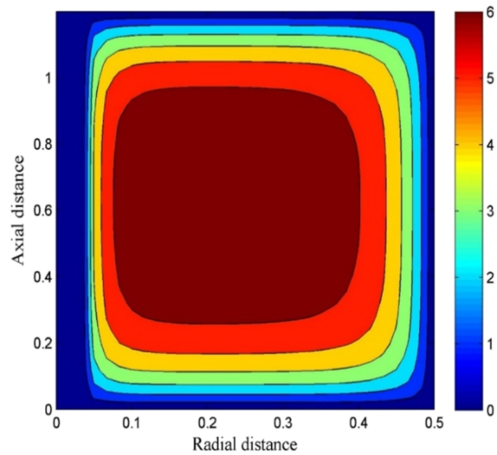

FIG. 4. Contour of air particles along both directions.

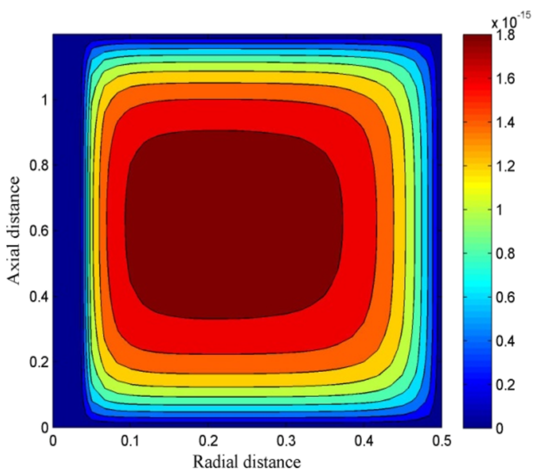

FIG. 5. Contour of dust particles along both directions.

of the fluid (air) for the radial position x = 24th of the tube along the axial distance (length of the tube), while the curve shown by the dotted line (blue) and the solid line (magenta) denote the axial velocity of fluid for the radial positions, x = 27th and x = 30th, respectively, of the tube along the axial distance (length of the tube).

Here, we found that as the position(x) of the tube along the axial direction (length of the tube) increases, the axial velocity of the fluid decreases.

Similarly, we also found that as the position(x) of the tube along the axial direction (length of the tube) increases, the axial velocity of the dust particles also decreases.

D. Effect of Reynolds number

Reynolds number (Re), a dimensionless parameter, plays a critical role in characterizing the nature of flow—whether laminar, transitional, or turbulent—especially in pipe-like geometries. In this study, the influence of axial velocities of both the carrier fluid (air)

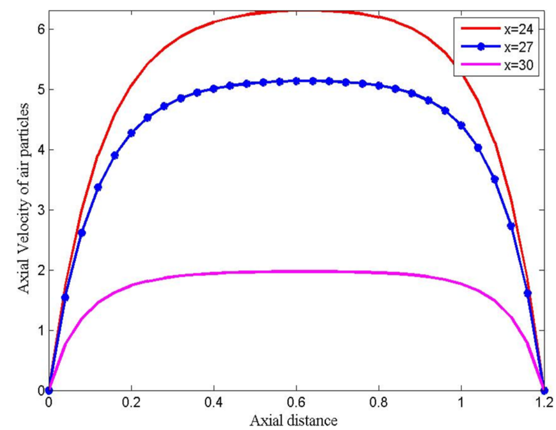

FIG. 6. Velocity variation of air particles along the axial direction.

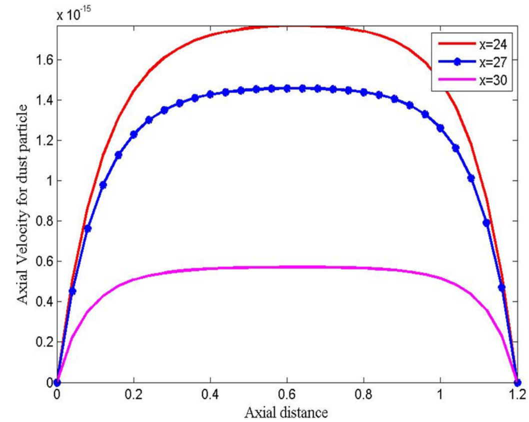

FIG. 7. Velocity variation of dust particles along the axial direction.

and suspended dust particles is analyzed for low Reynolds numbers ranging from 0.2 to 1. The simulations are conducted with parameters $D_a = 0.01$, $\varepsilon = 0.84$, $\alpha' = 12$, and $\beta = 10$. Figures 8 and 9 illustrate the streamline patterns and velocity distributions in the axial direction within a circular tube under rhythmic pulsatile flow conditions.

Figures 8 and 9 show that air and dust move faster as the Reynolds number increases from 0.2 to 1. This is because, at higher Reynolds numbers, the fluid's movement (inertia) becomes stronger than its resistance (viscosity).

At low Reynolds numbers, the flow is slow and smooth. However, as Re increases, the flow becomes faster and more active. The pulsating airflow and random motion of dust also help increase the speed.

This pattern matches how air flows in damaged lungs with emphysema, where the structure is more open and less resistant.

E. Effect of the Darcy number

The Darcy number (Da) is a dimensionless number used in fluid mechanics to describe the permeability of a porous medium.

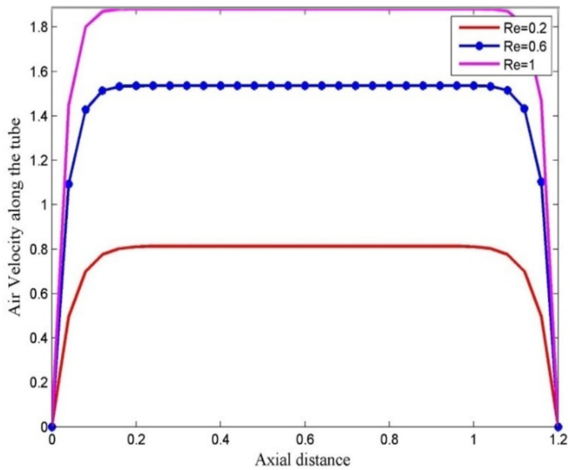

FIG. 8. Effect of the Reynolds number for air velocity in the axial direction.

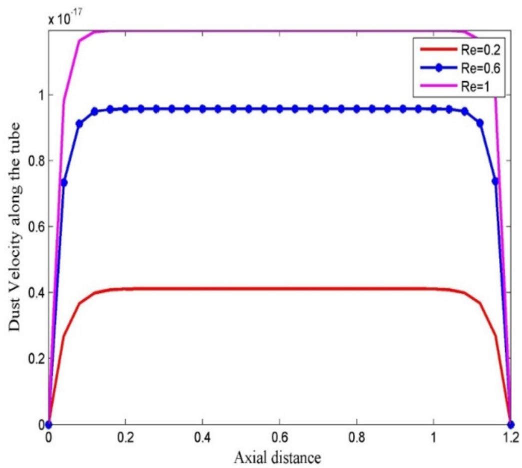

FIG. 9. Effect of the Reynolds number for dust velocity in the axial direction.

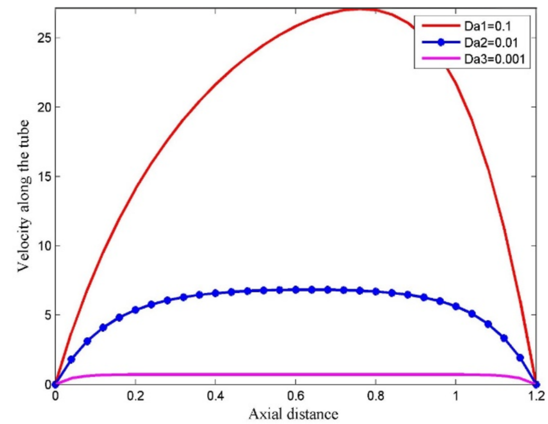

FIG. 10. Effect of the Darcy number for air velocity in the axial direction.

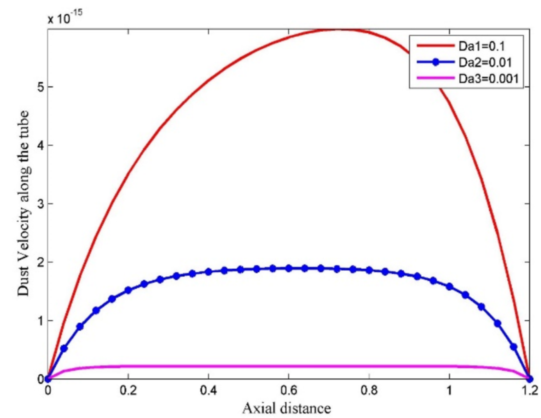

FIG. 11. Effect of the Darcy number for dust velocity in the axial direction.

It provides a measure of how easily a fluid can flow through the porous material. In Figs. 10 and 11, we can analysis the effect of Darcy number on flow regime at Re = 0.2, r = 100 nm, $\varepsilon = 0.84$, $\alpha' = 12$, and $\beta = 10$.

We noticed from the above-mentioned figure that the speed of air and dust molecules in the axial direction has a parabolic shape for all values of D_a and increases when D_a is increased from 0.001 to 0.1.

Finally, in this case, we can say that because of emphysema, air and particle velocity gradually increased as time passed. Since low drag forces are imparted to fluids during flow through highly porous media and since pressure gradients are likewise reduced, fluid velocity rises with respect to time by lowering the Darcy number. We can infer from this conclusion that highly porous media allow for more unrestricted airflow and that is why with increasing Darcy number, the axial velocity profile of air and dust particles also increases.

F. Effect of aspect ratio

Particle length to particle width is referred to as the aspect ratio (β). Since not every particle in the environment has an exact spherical shape, the aspect ratio is a crucial consideration accounting for nonspherical nanoparticles. Now, in the following figure, we see the dimensional distribution of velocity profile at various levels of aspect ratio such as $15 \le \beta \le 25$ and also for Re = 0.2, r = 100 nm, $\varepsilon = 0.84$, $\alpha' = 12$, and $D_a = 0.01$.

From Figs. 12 and 13, we noticed that when aspect ratio is low, velocity profile for air and dust is also low which is parabolic along axial distance. However, as the aspect ratio rises, so does the velocity profile, with an aspect ratio of 25 having a high-velocity profile for air and dust particles. This means that low aspect ratio particles are settled in earlier airways, whereas high aspect ratio particles travel deep inside the lung airways with the air stream.

G. Effect of porosity on normal lung and emphysema-affected lung

Figure 14 illustrates how lung porosity affects a healthy lung and an emphysematous lung. To determine the effect of emphysema

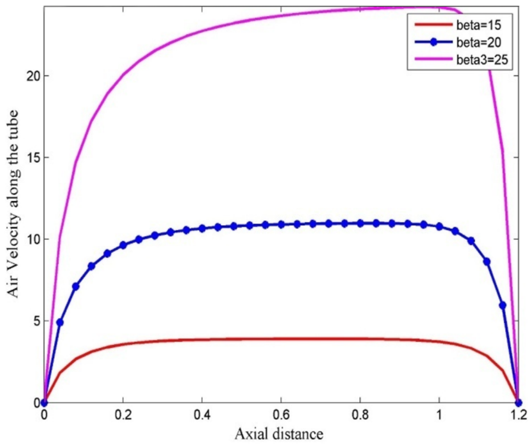

FIG. 12. Aspect ratio effect on the axial velocity of air particles.

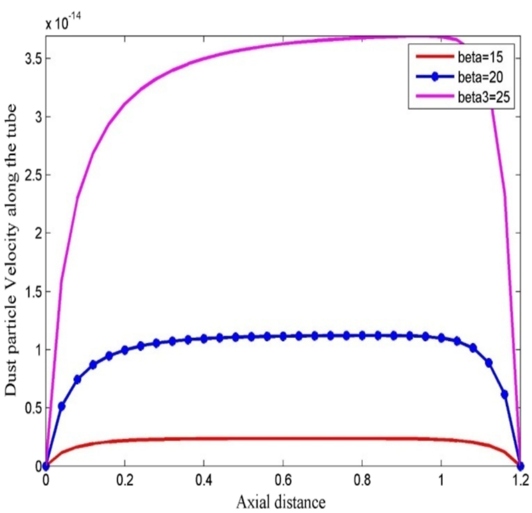

FIG. 13. Aspect ratio effect on the axial velocity of dust particles.

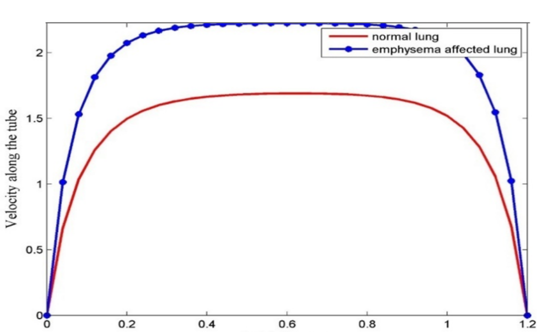

FIG. 14. Porosity effect on the axial velocity of fluid along the tube.

of air velocity on the axial direction at $\beta = 10$, $d = 100$ nm, and Re = 0.2, we employed porosity as a function of tidal volume.

We discovered that the axial velocity of air U_y increases along axial direction and it attains maximum value at y = 0.6 and then gradually decreases for an emphysema and a normal lung. From Fig. 14, we discover a normal lung travels more slowly than an emphysema-affected lung. Since highly permeable materials or materials with big pores make it easy for fluid to move; therefore, an emphysema-affected lung (compared to a normal lung) allows air to move more easily, yet medically, this behavior causes problems with rhythmic breathing.

VII. CONCLUSION

A list of the main conclusions of the analysis that was done in this work is presented in the following.

(1) Clearly, there is an inverse relationship between velocity and density. Velocity is reduced by an increase in density. Since dust particles have a more significant density ($0.025\,04 \times 10^{12}$ m^3) than air particles (1.145 kg/m^3), we can see from our study analysis of the velocity profiles of air and dust particles that dust velocity is lower than air speed.

(2) We found that the axial velocity of fluid and dust particles increased with increasing the radial position (diameter) of the tube.

(3) Increases in aspect ratio, Reynolds number, and Darcy number have been found to greatly enhance the velocity of air and dust particles.

(4) Particles with a low aspect ratio usually settle in the upper airways, while those with a high aspect ratio can travel deeper into the lungs along with the airflow.

(5) Finally, we found for highly porous media caused by emphysema that in this case, air and particle velocities are high. It has a great effect on normal breathing.

We discovered that the findings of the current investigation can be used to analyze the physical state of emphysema-affected lungs. It is also beneficial to understand the symptoms of conditions like asthma, chronic bronchitis, and chronic obstructive pulmonary disease (COPD).

AUTHOR DECLARATIONS

Conflict of Interest

The authors have no conflicts to disclose.

Author Contributions

Nilufar Yasmin: Conceptualization (lead); Data curation (lead); Formal analysis (lead); Investigation (lead); Methodology (lead); Software (lead); Validation (lead); Visualization (lead); Writing – original draft (equal); Writing – review & editing (equal). **Roni Akter**: Conceptualization (supporting); Software (supporting); Visualization (equal); Writing – review & editing (supporting). **Mst. Sathi Akter**: Conceptualization (supporting); Supervision (equal); Writing – review & editing (supporting). **Mahtab U. Ahmmed**: Formal analysis (supporting); Software (supporting); Supervision (equal).

DATA AVAILABILITY

Data sharing is not applicable to this article as no new data were created or analyzed in this study.

REFERENCES

[1]V. Subramaniyan *et al.*, "Introduction to lung disease," in *Targeting Epigenetics in Inflammatory Lung Diseases* (Springer, 2023), pp. 1–16.
[2]D. Han *et al.*, "A new multifunction oxygenator with a dual-chamber gas exchanger to reduce dependence on oxygen supply," ASAIO J. **71**, 719 (2025).
[3]G. He, T. Zhang, J. Zhang, B. Griffith, and Z. Wu, "Blood gas exchanger for multifunctional respiratory support," PCT/US2024/012927, 2024.
[4]M. Sankar, N. Girish, and Z. Siri, "Fully developed magnetoconvective heat transfer in vertical double-passage porous annuli," in *Flow and Transport in Subsurface Environment* (Springer, Singapore, 2018), pp. 217–249.
[5]M. K. Hasan and M. U. Ahmmad, "A numerical simulation of air flow in the human respiratory system based on lung," J. Appl. Math. Phys. **11**, 2205–2215 (2023).
[6]J. E. Hall and M. E. Hall, *Guyton and Hall Textbook of Medical Physiology E-Book* (Elsevier Health Sciences, 2020).
[7]O. Claris, C. Lapillonne, J. C. Picaud, and E. Basson, "High-frequency oscillatory ventilation," Semin. Neonatol. **2**(2), 129–137 (1997).
[8]M. S. Akter, M. U. Ahmmed, N. Y. Tanisa, and S. Hossain, "Deposition of nanoparticles through a cylindrical tube of human respiratory system," AIP Adv. **14**, 125320 (2024).
[9]A. Saini *et al.*, "Two-dimensional model of nanoparticle deposition in the alveolar ducts of the human lung," Appl. Appl. Math.: Int. J. **12**, 305–318 (2017).
[10]J. Kori, "Two dimensional mathematical study of flow dynamics through emphysemic lung," Appl. Appl. Math.: Int. J. **14**, 296–311 (2019) 19.
[11]K. M. Khanafer *et al.*, "The role of porous media in modeling fluid flow within hollow fiber membranes of the total artificial lung," J. Porous Media **15**, 113–122 (2012).
[12]J. Kori and Pratibha, "Effect of periodic permeability of lung tissue on fluid velocity and nonspherical nanoparticle filtration," Int. J. Appl. Comput. Math. **5**, 49 (2019).
[13]W.-C. Su and Y. S. Cheng, "Deposition of fiber in a human airway replica," J. Aerosol Sci. **37**(11), 1429–1441 (2006).
[14]J. T. Kelly *et al.*, "Particle deposition in human nasal airway replicas manufactured by different methods. Part II: Ultrafine particles," Aerosol Sci. Technol. **38**, 1072–1079 (2004).
[15]E. Weibel, "Morphometrics of the lung," in *Handbook of Applied Physiology* (American Physiological Society, 1964), Vol. 2, pp. 285–308.
[16]B. Haefeli-Bleuer and E. R. Weibel, "Morphometry of the human pulmonary acinus," Anat. Rec. **220**, 401–414 (1988).